

Isogeometric Analysis-Based Topological Optimization for Heterogeneous Parametric Porous Structures*

HU Chuanfeng · HU Hui · LIN Hongwei · YAN Jiacong

DOI: 10.1007/s11424-022-1290-6

Received: 11 August 2021 / Revised: 5 December 2021

©The Editorial Office of JSSC & Springer-Verlag GmbH Germany 2022

Abstract Porous structures widely exist in nature and artifacts, which can be exploited to reduce structural weight and material usage or improve damage tolerance and energy absorption. In this study, the authors develop an approach to design optimized porous structures with Triply Periodic Minimal Surfaces (TPMSs) in the framework of isogeometric analysis (IGA)-based topological optimization. In the developed method, by controlling the density distribution, the designed porous structures can achieve the optimal mechanical performance without increasing the usage of materials. First, the implicit functions of the TPMSs are adopted to design several types of porous elements parametrically. Second, to reduce the cost of computation, the authors propose an equivalent method to forecast the elastic modulus of these porous elements with different densities. Subsequently, the relationships of different porous elements between the elastic modulus and the relative density are constructed. Third, the IGA-based porous topological optimization is developed to obtain an optimal density distribution, which solves a volume constrained compliance minimization problem based on IGA. Finally, an optimum heterogeneous porous structure is generated based on the optimized density distribution. Experimental results demonstrate the effectiveness and efficiency of the proposed method.

Keywords B-spline solid, heterogeneous porous structure, isogeometric analysis, topological optimization, triply periodic minimal surface.

1 Introduction

The porous structure is a type of solid structure composed of a large number of interconnected pores, which widely exists in nature, including trabecular bone, wood and cork. These porous structures, formed via a natural evolution process for millions of years, exhibit exceptional physical properties at lightweight, damping enhancement^[1], damage tolerance^[2] and energy absorption^[3]. The porous materials have more extensive industrial application prospects than traditional single functional materials. Therefore, the porous materials have already been

HU Chuanfeng · HU Hui · LIN Hongwei · YAN Jiacong

School of Mathematical Sciences, State Key Lab. of CAD&CG, Zhejiang University, Hangzhou 310027, China.

Email: hwlin@zju.edu.cn.

*This research was supported by the National Natural Science Foundation of China under Grant Nos. 61872316 and 61932018, and the National Key R&D Plan of China under Grant No. 2020YFB1708900.

◇This paper was recommended for publication by Editor CHEN Shaoshi.

widely applied in many fields, for instance, the impact resistant structures in the field of energy absorption^[3], the porous tissue scaffolds in the field of tissue engineering^[4] and the catalyst structures in the field of chemistry engineering^[5].

The mechanical properties of porous structures are related not only to material type but also to the material distribution. Therefore, the material distribution of porous structures must be analysed and optimized to improve their mechanical properties. However, the state of the art^[6] is to optimize the density of the design domain without considering the structural properties of the porous structure and maps the optimized density directly into the infilled porous elements to generate a porous structure. The topological optimization is solved by finite element method (FEM), which reduces the calculation accuracy and increases the calculation time. Besides, the density in each analytic element is unified, which neglects the heterogeneity of the porous structure.

In this study, we presented a method to design optimized porous structures generated in a B-spline solid with Triply Periodic Minimal Surfaces (TPMSs) in the framework of isogeometric analysis (IGA)-based porous topological optimization. The porous structures can achieve desirable mechanical performance without increasing their weight by controlling the density distribution. Firstly, we first designed several types of porous elements with different densities by using the implicit functions of TPMSs. Secondly, we developed an equivalent method to calculate the equivalent elastic modulus of the porous elements on the basis of Energy Conservation Law. The equivalent elastic modulus is defined as the elastic modulus of a porous structure as a material. Then, we constructed the functional relationships of different porous elements between the equivalent elastic modulus and the relative density. Subsequently, given the design domain represented by a B-spline solid, boundary conditions and constraints, we obtained an optimal density distribution from the IGA-based porous topological optimization for minimising the compliance. Finally, we can construct an optimum porous structure in the B-spline solid with TPMS on the basis of the optimized density distribution. The proposed porous topological optimization method closely combines with the structural properties of TPMS-based porous materials. The density distribution represented by a trivariate B-spline function accurately reflects the heterogeneity of porous structures. The IGA-based method improves the calculation accuracy and efficiency. In summary, the main contributions of this study are as follows:

- An equivalent method is proposed to measure the structural properties of the porous materials.
- The equivalent elastic modulus of different TPMS-based porous materials is firstly considered in the porous topological optimization.
- The heterogeneity of porous structures is more accurately reflected by the density distribution represented by a trivariate B-spline function than the traditional methods.
- The IGA-based method is employed to improve the calculation accuracy and efficiency.

The remainder of this paper is organized as follows. In Section 1.1, we review related work on the porous structural design and topological optimization. In Section 2, preliminaries on trivariate B-spline solid and TPMS are introduced. In Section 3, TPMS-based porous structural design method is presented, and equivalent method for calculating equivalent elastic modulus of TPMS-based porous element is developed. In Section 4, the IGA-based topological optimization method for heterogeneous porous structures is showed. In Section 5, experimental examples illustrate the effectiveness and efficiency of the proposed method in optimising the design of heterogeneous porous structures. Section 6 concludes the paper.

1.1 Related Work

Porous structural design. Various methods have been developed to fabricate porous structures, which can be generally categorised into two classes according to the shape of the designed porous structures, namely, regular and irregular porous structural design methods. In the regular methods, Computer Aided Design (CAD)-based^[7], image-based^[8] and implicit surface-based^[9] methods are proposed to manufacture porous structures. On the contrary, the irregular methods are mainly composed of stochastic geometry-based^[10], stochastic modeling-based^[11] and Voronoi diagram-based^[12] methods. In particular, a standard parametric polyhedron model library was designed and developed in [7], from which users can select the element to construct porous structures. Sun, et al.^[8] converted trabecular structures on the basis of Computed Tomography (CT) into CAD models for designing bone scaffolds. To overcome the limitation of porous cell geometry in the construction of porous scaffolds, TPMS was firstly adopted to design porous scaffolds in [9]. Schroeder, et al.^[10] introduced the stochastic geometry theory into the porous structural modeling of tissue scaffolds. Sogutlu and Koc^[11] proposed a stochastic modeling method to obtain tissue scaffolds with controllable porosity. Kou and Tan^[12] developed an approach based on the Voronoi diagram and B-spline curve to design irregular porous structures with controllable pore shape and distribution. Owing to the excellent properties of TPMS, many TPMS-based porous structure design methods have been proposed^[13]. A method for designing porous structures based on signed distance field and TPMS is implemented in [14]. Yang, et al.^[15] proposed a method to obtain multimorphology porous structures based on hybridization of TPMSs. Hu and Lin^[16] presented a parametric porous scaffold design method of coupling trivariate B-spline solids and TPMSs, which improves design efficiency greatly. And a new file storage format of porous scaffold was proposed, which saves storage space significantly. Inspired by the representation of parametric porous structure design, we raised a topological optimization method for parametric porous structures.

Trivariate B-spline solid generation. In isogeometric analysis, tools such as B-splines are usually used for modeling in the physical domain. Specifically, trivariate B-spline solid modeling methods are developed mainly for three dimensional physical domain^[17]. Zhang, et al.^[18] introduced a skeleton-based method of generating trivariate NURBS solids for analyzing arterial blood flow through isogeometric analysis. Martin, et al.^[19] proposed a method to parameterize tetrahedral mesh models through discrete volumetric harmonic functions and a cylinder-like trivariate B-spline solid is generated. Chen, et al.^[20] presented a general framework

to construct volumetric parameterization from complex shapes. Xu, et al.^[21] developed a discrete mask method for the efficient construction of multi-block volumetric parameterization based on a set of given boundary spline surfaces. Aigner, et al.^[22] introduced a variational framework for generating NURBS parameterization of swept volumes using the given boundary conditions and guiding curves. Xu, et al.^[23] proposed a framework of computation reuse in IGA on a set of three-dimensional models with similar semantic features. To construct trivariate B-spline solids with positive Jacobian values, optimization approaches have been devised for filling boundary-represented models^[24, 25]. In addition, a discrete volume parameterization method for tetrahedral mesh models and an iterative fitting procedure have been provided for trivariate B-spline solid generation^[26].

IGA-based topological optimization. Topological optimization is a structural design tool based on mechanical principle and mathematical programming, which aims to determine the optimal density distribution for achieving the required performance under the given design domain, boundary conditions and constraints. To date, various methods in the framework of IGA are available to deal with topological optimization design problem, including density-based method^[27], phase field method^[28] and level set method^[29]. The IGA closely combines the geometric model information, avoids the meshing process, has high-order continuity and ensures geometric accuracy compared with the traditional FEM. Meanwhile, the IGA can effectively reduce the degree of freedom to solve the problem and improve the accuracy and efficiency of calculation and simulation^[30, 31].

The density-based method in topological optimization has an intuitive mathematical model, which is simple to implement and efficient in the calculation. Some work combined IGA and density-based methods to form the density-based topological optimization method in the framework of IGA. Hassani, et al.^[27] proposed an IGA-based topological optimization method combined with the optimization criteria method. They implemented an example of a 2D plane optimization problem, which shows that the proposed method can effectively suppress the checkerboard phenomenon. Qian^[32] presented a density-based topological optimization method based on B-spline function, introducing density distribution into B-spline function space. Liu, et al.^[33] developed an IGA-based design method to address the stress-constrained topological optimization problem of plane stress and bending of thin plates, which is derived from the popular SIMP (Solid Isotropic Material with Penalization) model.

Porous structural optimization. Various methods are presented for porous structural design based on topology optimization, which can be divided into two categories. On the one hand, the method generally optimizes the strut size or wall thickness^[34–36]. The structural and cell levels can be optimized by using this method; however, it is only applicable to some regular strut-based cellular structures. On the other hand, this method generally optimizes the material density distribution in the specific design domain. Brackett, et al.^[37] firstly proposed a SIMP-based density mapping approach to optimize the intermediate densities to 2D lattice structures of varying volume fraction. Ajit, et al.^[6] adopted the optimized density directly mapping into the infilled cellular structures. Wu, et al.^[38] established a self-supporting rhombic gradient infill topology design system for 3D printing object optimization. Li, et al.^[39] presented a method

to fill the model with graded gyroid TPMS porous structures, and the density of the structures depends on the local stress. Subsequently, compared to traditional topology optimization, Li, et al.^[40] improved the manufacturability of the model by modifying the optimization constraints according to different situations. Ajit, et al.^[6] introduced a large number of strategies for adopting the optimized density directly mapping into the infilled TPMS cellular structures, and it took into account mechanical properties and manufacturability through 3D printing. Besides, homogenization-based topological optimization methods are implemented to design porous structures in [41–43].

2 Preliminaries

Preliminaries on the trivariate B-spline solid and TPMS are introduced in this section.

2.1 Trivariate B-Spline Solid

In our study, the specific design domain is represented by a trivariate B-spline solid, which represents geometry at a macro-structural scale. A trivariate B-spline solid of degree (p, q, r) is a tensor product volume defined as

$$P(u, v, w) = \sum_{i=0}^m \sum_{j=0}^n \sum_{k=0}^l N_{i,p}(u) N_{j,q}(v) N_{k,r}(w) P_{ijk}, \tag{1}$$

where P_{ijk} , $i = 0, 1, \dots, m$, $j = 0, 1, \dots, n$, $k = 0, 1, \dots, l$ are control points in the u , v and w directions, and

$$N_{i,p}(u), N_{j,q}(v), N_{k,r}(w)$$

are the B-spline basis functions of degree p in the u direction, degree q in the v direction and degree r in the w direction, with parametric domain $[0, 1] \times [0, 1] \times [0, 1]$.

$$R_{ijk} = N_{i,p}(u) N_{j,q}(v) N_{k,r}(w) \tag{2}$$

is the blending basis function.

2.2 Triply Periodic Minimal Surface





TPMS is an implicit surface that infinitely extends along with three independent directions in Euclidean space, portioning the area into two labyrinths, and non-self-intersection, which is a competitive tool for designing porous structures. The TPMS can be evaluated through several ways, and the frequently employed approach is to approximate the TPMS by using a periodic nodal surface defined by a Fourier series ^[44],

$$\psi(\mathbf{r}) = \sum_k A_k \cos[2\pi(\mathbf{h}_k \cdot \mathbf{r})/\lambda_k - P_k] = C, \tag{3}$$

where \mathbf{r} is the location vector in the Euclidean space, A_k is the amplitude, \mathbf{h}_k is the k th lattice vector in the reciprocal space, λ_k is the wavelength of the period, P_k is the phase shift and C is

the threshold constant. The nodal approximations of four types (P, D, G and I-WP) of TPMSs are listed in Table 1. Coefficients α_u , α_v and α_w , called period coefficients, affect the period of the TPMS and the pore size. TPMSs in a complete period are presented in Table 1, which are extracted by marching tetrahedra (MT) algorithm^[45].

Table 1 Typical examples of TPMSs

TPMS	Mathematical expression	Model
P	$\psi_P(u, v, w) = \cos(\alpha_u u) + \cos(\alpha_v v) + \cos(\alpha_w w) = 0.9C$	
D	$\psi_D(u, v, w) = \cos(\alpha_u u) \cos(\alpha_v v) \cos(\alpha_w w) - \sin(\alpha_u u) \sin(\alpha_v v) \sin(\alpha_w w) = 0.6C$	
G	$\psi_G(u, v, w) = \sin(\alpha_u u) \cos(\alpha_v v) + \sin(\alpha_v v) \cos(\alpha_w w) + \sin(\alpha_w w) \cos(\alpha_u u) = 0.9C$	
I-WP	$\psi_{I-WP}(u, v, w) = \cos(2\alpha_u u) + \cos(2\alpha_v v) + \cos(2\alpha_w w) - 2[\cos(\alpha_u u) \cos(\alpha_v v) + \cos(\alpha_v v) \cos(\alpha_w w) + \cos(\alpha_w w) \cos(\alpha_u u)] = 2.5C$	

The threshold constant C is defined in $[-1, 1]$ to guarantee that the implicit surface is continuous.

3 Parameterisation of Porous Structural Properties

In this study, the proposed method firstly generates a TPMS-based porous structure within a cuboid, which is the parametric domain of a trivariate B-spline solid. Then, a vivid porous model is obtained by mapping the generated porous structure into the trivariate B-spline solid. In this section, four typical TPMS-based porous elements for designing porous structures are presented, and the heterogeneous porous structural generation method is introduced. Moreover, the equivalent elastic modulus of the porous elements with relative density is defined, which is adopted in the porous structural topological optimization.

3.1 TPMS-Based Porous Element

In our implementation, the four TPMSs (P, D, G and I-WP) are used to design four types of TPMS-based porous elements, which are shown in Figure 1.

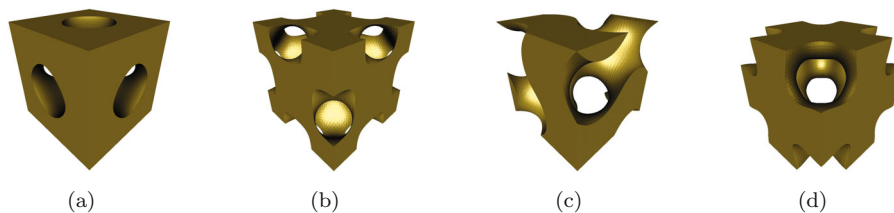


Figure 1 Four types of TPMS-based porous elements. (a) P-type. (b) D-type. (c) G-type. (d) I-WP-type

As stated above, the pore size is controlled by the threshold C . Therefore, the material usage (i.e., the relative material density) of porous elements can be controlled by the threshold C . To construct the relationships between the relative density and the threshold constant C of the four types of porous elements, we sample uniformly in the range of $[-1, 1]$ to obtain multiple sets of the threshold C . By substituting the multiple sets of threshold C into the expressions of the four type of TPMSs, multiple porous elements can be generated. Subsequently, the relative material density of porous elements is calculated, and the scatter plot is drawn, as shown in Figure 2. Finally, for each type of TPMS porous element, the function between the relative density and the threshold constant C is established by data fitting, which is presented in Appendix A.

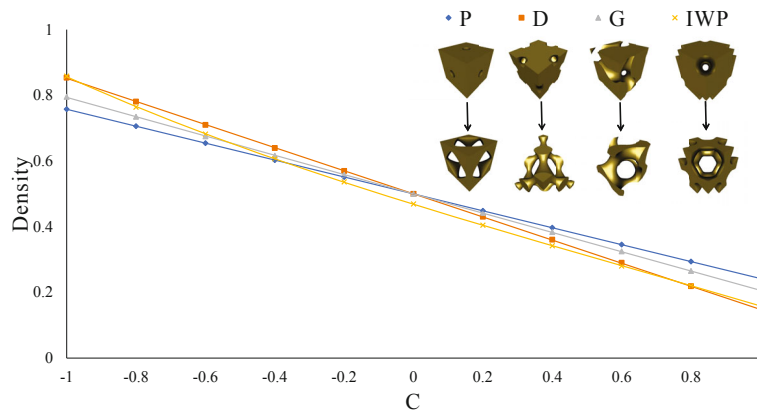


Figure 2 Relationship between the relative density and the threshold C of the four types of TPMS-based porous elements

3.2 Heterogeneous TPMS-Based Porous Structure

To generate heterogeneous TPMS-based porous structures, the threshold constant C is modified as a scalar function: $C(u, v, w)$. This notion means that each value of $C(u, v, w)$ determines the density of a certain point $(u, v, w) \in R^3$. In this study, the scalar function is represented by a trivariate B-spline function (4) to achieve a highly complex density distribution,

$$C(u, v, w) = \sum_{i=0}^m \sum_{j=0}^n \sum_{k=0}^l N_{i,p}(u) N_{j,q}(v) N_{k,r}(w) C_{ijk}. \tag{4}$$

Now, we can start designing a heterogeneous TPMS-based porous structure. We firstly generate a TPMS-based porous structure within a cuboid, which is the parametric domain of a trivariate B-spline solid. The pore number can be controlled by the period coefficients. Then, a heterogeneous porous structure is generated by mapping the porous structure in the parametric domain into the B-spline solid. Figure 3(a) shows an example of a linear grading for a P-type porous structure where C varies from -1 at the bottom to 1 at the top, and the corresponding porous structure in the B-spline solid is shown in Figure 3(b). Moreover, the heterogeneous

parametric porous structure can be expressed by coupling parametric solid spline function and parametric implicit surface function.

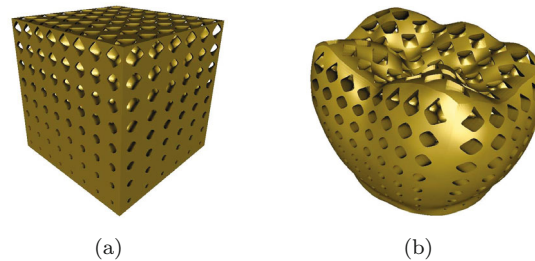


Figure 3 TPMS-based heterogeneous parametric porous structure. (a) Porous structure in the parametric domain. (b) Porous structure in a B-spline solid

3.3 Equivalent Method

To establish the relationship between density and stress considering the structural properties of porous materials, we develop an equivalent method to calculate the equivalent elastic modulus of different TPMS-based porous materials by FEM on the basis of Energy Conservation Law. Then, we establish the functional relationships between the density and the equivalent elastic modulus of different porous materials. In Figure 4, we show the basic principle of the equivalent method for calculating the equivalent elastic modulus of porous materials. Specifically, suppose a porous domain Ω^p is infilled with porous elements, subjected to a fixed boundary face, and a body force is distributed in the domain. The porous structure is regarded as a hexahedral domain Ω^h , and the porous elements are equivalently replaced by hexahedral elements for finite element analysis, which significantly reduces the degree of freedom.

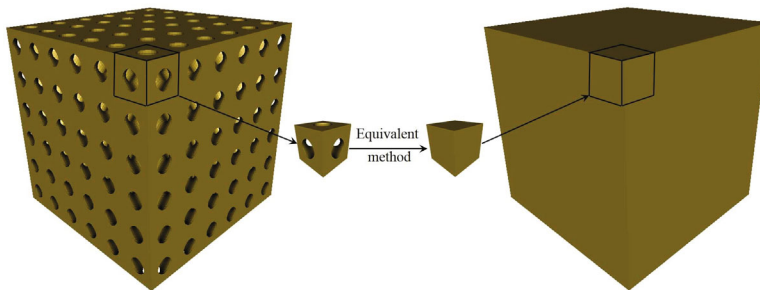


Figure 4 Equivalent method. The left side is a P-type porous structure Ω^p with six elements in three periodic directions. The right side is a uniform hexahedral mesh Ω^h with the same number of elements

In terms of linear elasticity, the expression of the total potential energy produced by the body force is as follows:

$$c = \mathbf{U}^T \mathbf{K} \mathbf{U} = \sum_{e=1}^{N_e} \mathbf{U}_e^T \mathbf{K}_e \mathbf{U}_e, \quad (5)$$

where \mathbf{U} denotes the displacement, and \mathbf{K} represents the global stiffness matrix. Variables \mathbf{U}_e and \mathbf{K}_e are the element displacement and stiffness matrix, respectively, and N_e is the number of analysis elements. The global stiffness matrix can be assembled by the element stiffness matrices as follows,

$$\mathbf{K} = \sum_{e=1}^{N_e} \mathbf{K}_e = \sum_{e=1}^{N_e} \int_{\Omega_e} \mathbf{B}_e^T \mathbf{D} \mathbf{B}_e d\Omega_e, \tag{6}$$

where \mathbf{B}_e is the element strain-displacement matrix, \mathbf{D} is the constitutive matrix and Ω_e is the domain of the e th analytic element.

The equivalent elastic modulus of porous materials is calculated by the equivalent method, which assumes that the total potential energy produced by body force is equivalent in the porous domain Ω^p and the hexahedral domain Ω^h . Therefore, Equation (5) can be transformed into the following form,

$$\sum_{e=1}^{N_e^p} \mathbf{U}_e^p{}^T \mathbf{K}_e^p \mathbf{U}_e^p = \frac{E^*}{E} \sum_{e=1}^{N_e^h} \mathbf{U}_e^h{}^T \mathbf{K}_e^h \mathbf{U}_e^h, \tag{7}$$

where \mathbf{U}_e^p and \mathbf{K}_e^p are the element displacement and stiffness matrix, respectively; and N_e^p is the number of analysis elements in the domain infilled with porous structures. Variables \mathbf{U}_e^h , \mathbf{K}_e^h and N_e^h are the variables in the equivalent hexahedral domain. Additionally, E is Young’s modulus of actual material, E^* is the equivalent elastic modulus of porous material and E^*/E is defined as the equivalent ratio of elastic modulus.

We can obtain \mathbf{U}_e^p by solving the following static equilibrium equation:

$$\mathbf{M} = \mathbf{K} \mathbf{U} = \sum_{e=1}^{N_e^p} \mathbf{K}_e^p \mathbf{U}_e^p, \tag{8}$$

where \mathbf{M} is the body force. Subsequently, \mathbf{U}_e^h can be calculated by weighting the displacements of its equivalent porous element. Suppose that an equivalent porous element consists of n_e analysis elements in the porous domain Ω^p , we have

$$\mathbf{U}_e^h = \frac{\sum_{t=1}^{n_e} Vol(\Omega_t^p) \mathbf{U}_t^p}{\sum_{t=1}^{n_e} Vol(\Omega_t^p)}, \tag{9}$$

where Ω_t^p is a discretized analysis element in the porous domain Ω^p , and $Vol(\cdot)$ is a volume function. In fact, we need to calculate the displacement of the porous element by the displacement on the node of tetrahedrons. And then by uniformly distributing the displacement of the porous element to the node of the hexahedron, \mathbf{U}_e^h is established. Finally, we can obtain the equivalent ratio of elastic modulus E^*/E from Equation (7).

We draw a scatter diagram as shown in Figure 5 by calculating the values E^*/E of different porous materials with different densities and establish the functional relationships between the equivalent ratio of elastic modulus and the relative material density for four different TPMS-based porous structures. The mathematical functions are presented in Appendix B.

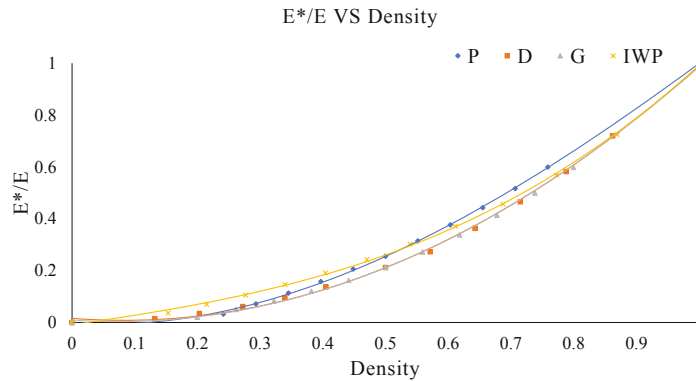


Figure 5 Relationship between the equivalent ratio of elastic modulus and the relative material density of the four types of TPMS-based porous structures

4 IGA-Based Porous Topological Optimization

Structural topological optimization was firstly proposed in the 1980s, and the motivation is to design lightweight structures^[46]. The SIMP method^[47] is one of the widely used optimization algorithms. The method has an intuitive mathematical model, simple to implement and efficient in the calculation. In this study, IGA-based SIMP is employed to optimize the density distribution in consideration of the structural properties of the porous structures, thus achieving optimal mechanical performance.

4.1 IGA-Based Design Parameterisation

IGA is a new high-order numerical method of FEM, which closely combines the geometric description and simulation analysis. In comparison with the traditional FEM, IGA has the advantages of geometric accuracy and high-order continuity between elements, which improves the accuracy and credibility of structural analysis. In structural analysis, the displacement distribution is expressed as

$$U(u, v, w) = \sum_{i=0}^m \sum_{j=0}^n \sum_{k=0}^l N_{i,p}(u) N_{j,q}(v) N_{k,r}(w) U_{ijk}, \quad (10)$$

where U_{ijk} is the displacement of the control points P_{ijk} .

The B-spline parameterisation method is employed to construct the relative material density distribution for the IGA-based topological optimization in the SIMP-framework. In each control point P_{ijk} of the B-spline solid, an extra density control scalar ρ_{ijk} is added. A density scalar distribution is represented by a trivariate B-spline function:

$$\rho(u, v, w) = \sum_{i=0}^m \sum_{j=0}^n \sum_{k=0}^l N_{i,p}(u) N_{j,q}(v) N_{k,r}(w) \rho_{ijk}. \quad (11)$$

4.2 Objective Function

In this study, the topological optimization problem is formulated by minimising the compliance of the porous structures, which is expressed with IGA-based discretisation as

$$\begin{aligned}
 \min_{\rho_{ijk}} \quad & c(\rho_{ijk}) = \mathbf{U}^T \mathbf{K} \mathbf{U} \\
 \text{s.t.} \quad & \mathbf{K} \mathbf{U} = \mathbf{F}, \\
 & V = \int_{\Omega} \rho d\Omega = \tau Vol(\Omega), \\
 & \rho_{\min} \leq \rho_{ijk} \leq \rho_{\max},
 \end{aligned} \tag{12}$$

where ρ_{ijk} is design variables; \mathbf{F} is the external force vector; τ is the given target volume fraction; Ω is the design domain; and ρ_{\min}, ρ_{\max} are the minimum and maximum density values, respectively. The stiffness matrix \mathbf{K} is defined as follows:

$$\mathbf{K} = \begin{bmatrix} \mathbf{K}_{11} & \mathbf{K}_{12} & \mathbf{K}_{13} \\ \mathbf{K}_{21} & \mathbf{K}_{22} & \mathbf{K}_{23} \\ \mathbf{K}_{31} & \mathbf{K}_{32} & \mathbf{K}_{33} \end{bmatrix}, \tag{13}$$

where the submatrices $\mathbf{K}_{11}, \mathbf{K}_{12}, \mathbf{K}_{13}, \mathbf{K}_{21}, \mathbf{K}_{22}, \mathbf{K}_{23}, \mathbf{K}_{31}, \mathbf{K}_{32}$ and \mathbf{K}_{33} are obtained with entries from following integrals by means of Gaussian quadrature rules^[48]:

$$\left\{ \begin{aligned}
 \{\mathbf{K}_{11}\}_{ij} &= \int_{\Omega} (\lambda + \mu) \frac{\partial \mathcal{R}_i}{\partial x} \frac{\partial \mathcal{R}_j}{\partial x} + \mu \frac{\partial \mathcal{R}_i}{\partial y} \frac{\partial \mathcal{R}_j}{\partial y} + \mu \frac{\partial \mathcal{R}_i}{\partial z} \frac{\partial \mathcal{R}_j}{\partial z} d\Omega, \\
 \{\mathbf{K}_{12}\}_{ij} &= \int_{\Omega} \lambda \frac{\partial \mathcal{R}_i}{\partial x} \frac{\partial \mathcal{R}_j}{\partial y} + \mu \frac{\partial \mathcal{R}_i}{\partial y} \frac{\partial \mathcal{R}_j}{\partial x} d\Omega, \\
 \{\mathbf{K}_{13}\}_{ij} &= \int_{\Omega} \lambda \frac{\partial \mathcal{R}_i}{\partial x} \frac{\partial \mathcal{R}_j}{\partial z} + \mu \frac{\partial \mathcal{R}_i}{\partial z} \frac{\partial \mathcal{R}_j}{\partial x} d\Omega, \\
 \{\mathbf{K}_{21}\}_{ij} &= \int_{\Omega} \lambda \frac{\partial \mathcal{R}_i}{\partial y} \frac{\partial \mathcal{R}_j}{\partial x} + \mu \frac{\partial \mathcal{R}_i}{\partial x} \frac{\partial \mathcal{R}_j}{\partial y} d\Omega, \\
 \{\mathbf{K}_{22}\}_{ij} &= \int_{\Omega} (\lambda + \mu) \frac{\partial \mathcal{R}_i}{\partial y} \frac{\partial \mathcal{R}_j}{\partial y} + \mu \frac{\partial \mathcal{R}_i}{\partial x} \frac{\partial \mathcal{R}_j}{\partial x} + \mu \frac{\partial \mathcal{R}_i}{\partial z} \frac{\partial \mathcal{R}_j}{\partial z} d\Omega, \\
 \{\mathbf{K}_{23}\}_{ij} &= \int_{\Omega} \lambda \frac{\partial \mathcal{R}_i}{\partial y} \frac{\partial \mathcal{R}_j}{\partial z} + \mu \frac{\partial \mathcal{R}_i}{\partial z} \frac{\partial \mathcal{R}_j}{\partial y} d\Omega, \\
 \{\mathbf{K}_{31}\}_{ij} &= \int_{\Omega} \lambda \frac{\partial \mathcal{R}_i}{\partial z} \frac{\partial \mathcal{R}_j}{\partial x} + \mu \frac{\partial \mathcal{R}_i}{\partial x} \frac{\partial \mathcal{R}_j}{\partial z} d\Omega, \\
 \{\mathbf{K}_{32}\}_{ij} &= \int_{\Omega} \lambda \frac{\partial \mathcal{R}_i}{\partial z} \frac{\partial \mathcal{R}_j}{\partial y} + \mu \frac{\partial \mathcal{R}_i}{\partial y} \frac{\partial \mathcal{R}_j}{\partial z} d\Omega, \\
 \{\mathbf{K}_{33}\}_{ij} &= \int_{\Omega} (\lambda + \mu) \frac{\partial \mathcal{R}_i}{\partial z} \frac{\partial \mathcal{R}_j}{\partial z} + \mu \frac{\partial \mathcal{R}_i}{\partial y} \frac{\partial \mathcal{R}_j}{\partial y} + \mu \frac{\partial \mathcal{R}_i}{\partial x} \frac{\partial \mathcal{R}_j}{\partial x} d\Omega,
 \end{aligned} \right. \tag{14}$$

where \mathcal{R} is the blending basis functions of Equation (2), which can be arranged into a vector in lexicographical order, and the indices are the serial numbers in lexicographical order. Variables λ and μ are lame parameters defined as follows:

$$\lambda = \frac{E^* \nu}{(1 + \nu)(1 - 2\nu)}, \quad \mu = \frac{E^* \nu}{2(1 + \nu)}, \quad (15)$$

where ν is Poisson ratio of the actual material, and E^* is the equivalent elastic modulus of porous materials, which can be calculated according to the relative material density ρ and Young's modulus E of the actual material (Appendix B). In our implementation, we assume Young's modulus of 2.15 GPa and Poisson ratio of 0.3.

4.3 Sensitivity Analysis

For simplicity, the gradient-based standard Optimality Criteria (OC) method^[47] is adopted to perform topological optimization; thus, the first-order sensitivity information of the objective function is required. The derivative of structural compliance with respect to the density control scalar ρ_{ijk} is

$$\frac{\partial c}{\partial \rho_{ijk}} = \mathbf{U}^T \frac{\partial \mathbf{K}}{\partial \rho_{ijk}} \mathbf{U}. \quad (16)$$

In Equation (14), only λ and ν are related to the density distribution. We only need to calculate the derivative of equivalent elastic modulus E^* with respect to the density control scalar ρ_{ijk} ,

$$\frac{\partial E^*}{\partial \rho_{ijk}} = \frac{dE^*}{d\rho} \frac{\partial \rho}{\partial \rho_{ijk}} = \frac{dE^*}{d\rho} \mathcal{R}_{ijk}, \quad (17)$$

where $\frac{dE^*}{d\rho}$ can be easily calculated according to Appendix B. The derivative of compliance with respect to ρ_{ijk} can be calculated by the chain rule. In addition, the derivative of volume with respect to ρ_{ijk} is shown as follows,

$$\frac{\partial V}{\partial \rho_{ijk}} = \int_{\Omega} \mathcal{R}_{ijk} d\Omega. \quad (18)$$

In this study, a heuristic updating scheme employed for the design variables is formulated as,

$$\rho_{ijk}^{new} = \begin{cases} \max(\rho_{\min}, \rho_{ijk} - m), & \text{if } \rho_{ijk} B_{ijk}^{\eta} \leq \max(\rho_{\min}, \rho_{ijk} - m), \\ \min(\rho_{\max}, \rho_{ijk} + m), & \text{if } \min(\rho_{\max}, \rho_{ijk} + m) \leq \rho_{ijk} B_{ijk}^{\eta}, \\ \rho_{ijk} B_{ijk}^{\eta}, & \text{otherwise,} \end{cases} \quad (19)$$

where m is a positive move-limit, and η is a numerical damping coefficient. In our implementation, m and η are set as 0.1 and 0.5, respectively. B_{ijk} is found from the optimality condition^[47] as

$$B_{ijk} = \frac{-\frac{\partial c}{\partial \rho_{ijk}}}{\omega \frac{\partial V}{\partial \rho_{ijk}}},$$

where ω is a Lagrangian multiplier that can be obtained by a bi-sectioning algorithm.

The terminate condition for the porous topological optimization is as follows,

$$\|\rho_{ijk}^{new} - \rho_{ijk}\|_{\infty} < \varepsilon. \tag{20}$$

In our implementation, ε is set as 0.01.

4.4 Density Preservation and Porous Structure Generation

An optimized density distribution is obtained after the porous topological optimization. Then, we can construct the heterogeneous porous structure on the basis of the optimized density distribution. According to the functional relationship between the relative density and the threshold constant, a threshold distribution is established by directly mapping the density control scalar ρ_{ijk} into the threshold control scalar C_{ijk} (Appendix A). Subsequently, we can extract a porous structure in the parametric domain. Accordingly, a heterogeneous porous structure is generated by mapping the porous structure in the parametric domain into the B-spline solid using Equation (1), thus achieving the mechanical requirements.

To ensure that the density distribution after the B-spline solid mapping Equation (1) is consistent with the optimized density distribution, we develop a density preservation scheme. We can omit the process of density preservation if the B-spline solid mapping is linear. However, the trivariate B-spline function Equation (1) is generally nonlinear, thereby resulting in varying density distribution before and after the mapping. Therefore, a post-processing operation is necessary for the threshold distribution to ensure that the generated heterogeneous porous structure meets the optimized density distribution.

Suppose that the relative material density values at the center of porous elements $(x_{\ell}, y_{\ell}, z_{\ell})$, $\ell = 0, 1, \dots, \mathcal{M}$ in the B-spline solid are ρ_{ℓ} , whose corresponding parameters are $(u_{\ell}, v_{\ell}, w_{\ell})$. A constrained optimization objective function Equation (21) is formulated to ensure that the porous structure meets the density requirements. The optimization variables of the objective function are the control scalars of the threshold distribution, which are arranged in a vector $\{C_i, i = 0, 1, \dots, \mathcal{N}\}$.

$$\begin{aligned} \min \quad & \Pi = \sum_{\ell=0}^{\mathcal{M}} \|\rho(C_0, C_1, \dots, C_{\mathcal{N}}; u_{\ell}, v_{\ell}, w_{\ell}) - \rho_{\ell}\|^2 \\ \text{s.t.} \quad & C_0, C_1, \dots, C_{\mathcal{N}} \in [-1, 1]. \end{aligned} \tag{21}$$

The gradient descent method is applied to perform the minimisation optimization. The gradient vector of the objective function is,

$$\nabla \Pi = \left(\frac{\partial \Pi}{\partial C_0}, \dots, \frac{\partial \Pi}{\partial C_i}, \dots, \frac{\partial \Pi}{\partial C_{\mathcal{N}}} \right), \tag{22}$$

which can be calculated by the difference method, shown as follows,

$$\frac{\partial \Pi}{\partial C_i} = \frac{\Pi(\cdots, C_i + \delta, \cdots) - \Pi(\cdots, C_i, \cdots)}{\delta}, \quad (23)$$

$$i = 0, 1, \cdots, \mathcal{N},$$

where δ is a tiny increment, which is taken as 0.02 in our implementation.

The calculation of the relative density ρ in the heterogeneous porous structure is performed in the parametric domain. Therefore, the heterogeneous porous structure in the B-spline solid is not required to be generated.

In the optimization, the control scalars $\{C_i, i = 0, 1, \cdots, \mathcal{N}\}$ move along the gradient vector to produce the new control scalars, that is,

$$C_i = C_i - \varepsilon \frac{\partial \Pi}{\partial C_i}, \quad i = 0, 1, \cdots, \mathcal{N}, \quad (24)$$

where $\varepsilon \in (0, 1]$ is a weight. In our implementation, we discretise $\varepsilon \in (0, 1]$ to $\{\frac{1}{t}, \frac{2}{t}, \cdots, \frac{t}{t}\}$, set t to 20 and select a weight as large as possible to minimise the objective function Equation (21).

Finally, an optimized threshold distribution is obtained, and we can construct the porous structure in the parametric domain on the basis of the distribution. It can be formulated as,

$$\psi(u, v, w) = \sum_{i=0}^m \sum_{j=0}^n \sum_{k=0}^l N_{i,p}(u) N_{j,q}(v) N_{k,r}(w) C_{ijk}. \quad (25)$$

Subsequently, the heterogeneous porous structure can be generated through the B-spline solid mapping Equation (1), which achieves the specific mechanical requirements.

5 Implementation, Results and Discussions

The developed IGA-based topological optimization method for the heterogeneous parametric porous structure is implemented with the C++ programming language and tested on a PC with a 3.60 GHz i7-4790 CPU and 16 GB RAM. In this section, several examples are presented, and some implementation details are discussed. Moreover, the developed method is compared with the state of the art^[6].

5.1 Equivalent Method Estimation

In this subsection, the effectiveness of the proposed equivalent method for analysing the structural properties of porous elements is discussed. In Figure 6(a), we employ a cubic block of $1 \times 1 \times 1 \text{ cm}^3$ as a benchmark to study the effect of the porous element size on the equivalent method. The bottom of the cube is fixed, and an external force of 1000 N is applied to the upper face of the cube. The cube is infilled with P-type porous elements, and the relative density equals 0.5. Accordingly, a static equilibrium problem has arisen. The porous structures with different numbers of P-type porous elements are simulated to estimate the influence of porous element size on the equivalent method.

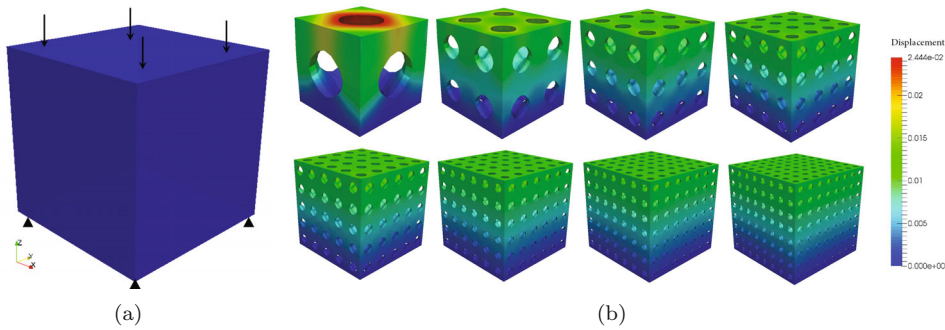


Figure 6 Equivalent method estimation. (a) Design domain with boundary conditions. (b) Actual FEM simulation results of different porous sizes (color represents the displacement)

The static equilibrium problem of the cube infilled with porous elements are solved by the actual FEM simulation and equivalent FEM simulation. Specifically, for the actual FEM simulation, each porous element is discretized into a tetrahedral mesh, and the Young’s modulus in the stiffness matrix is the Young’s modulus of the actual materials. By solving the static equilibrium equation, we can obtain the actual displacement caused by the external forces. For the equivalent FEM simulation, each porous element is replaced by a hexahedron, and the Young’s modulus in the stiffness matrix is the equivalent elastic modulus of the porous element (refer to Subsection 3.3). Therefore, the degree of freedom will be drastically reduced, and the equivalent displacement can be efficiently calculated. In Figure 6(b), the actual FEM simulation result is demonstrated, with displacement shown in color.

With regard to the cube infilled with P-type porous elements of different sizes, we employed actual and equivalent FEM for simulation. Therefore, we can calculate the compliance value according to Equation (5). The relative error of compliance is defined as follows:

$$error = \frac{c_a - c_e}{c_a}, \tag{26}$$

where c_a and c_e are the compliance of actual and equivalent FEM simulation, respectively. We also calculated the time cost of simulation. And the ratio of time cost is defined as follows:

$$ratio = \frac{T_a}{T_e}, \tag{27}$$

where T_a and T_e are the time cost of actual and equivalent FEM simulation, respectively. In Figure 7, the relative error of compliance and the ratio of time cost with respect to different porous element sizes are in blue and orange, respectively. The equivalent method can effectively approximate the actual FEM with the decrease in microporous size. The degree of freedom of the model will exponentially increase with the decrease in the microporous size, and the time cost of the actual FEM simulation will increase dramatically. Accordingly, the equivalent method

can effectively avoid the explosion of time cost.

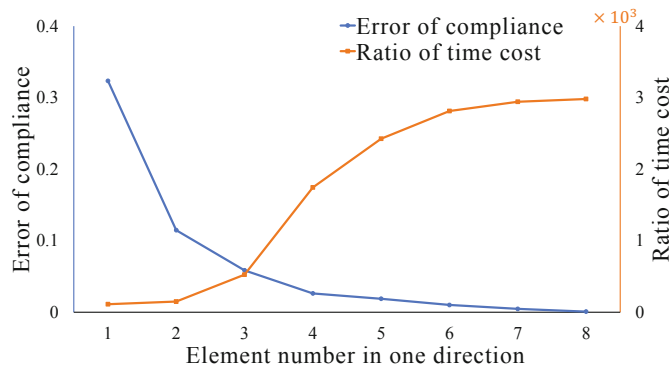


Figure 7 Relative error of compliance and ratio of time cost associated with porous element number in one direction

5.2 Regular Porous Domain

In this subsection, we employ two classic beams to the porous topological optimization for demonstrating the effectiveness of the developed method.

In Figure 8(a), an external force of 1000 N is initially distributed over the cantilever beam, and the left boundary face is fixed. The cantilever beam of $4 \times 2 \times 2 \text{ cm}^3$ is represented as a trivariate B-spline solid with a control grid of $21 \times 11 \times 11$ and degree of $2 \times 2 \times 2$. The P-type porous element is employed for optimization. In the optimization, ρ_{\min} and ρ_{\max} are set to 0.25 and 0.75, respectively. The target volume fraction τ is set to 0.4. After the porous topological optimization, we obtain the optimized density distribution (Figure 8(b)). Finally, the optimized heterogeneous porous cantilever beam infilled with $14 \times 7 \times 7$ P-type porous elements is generated (Figure 8(c)). The cross-sectional view (Figure 8(d)) of the optimized heterogeneous porous cantilever beam shows that the porous elements are smoothly connected, which indicates that the mechanical properties will not change singularly in the connection of porous elements.

The Messerschmitt-Bölkow-Blohm (MBB) beam is adopted to the porous topological optimization shown in Figure 9. In Figure 9(a), the middle position of the upper part of the beam is subjected to an external force of 1000 N, a rolling hinge constrains the lower right part, and the lower left part is fixed. The MBB beam of $6 \times 2 \times 2 \text{ cm}^3$ is represented as a trivariate B-spline solid with a control grid of $31 \times 11 \times 11$ and degree of $2 \times 2 \times 2$. Additionally, the D-type porous element with a density of 0.15 to 0.85 intervals is employed to infill the design domain. The target volume fraction τ is set to 0.3. The optimized density distribution after the porous topological optimization is shown in Figure 9(b). Finally, we construct the heterogeneous porous MBB beam infilled with $21 \times 7 \times 7$ D-type porous elements (Figure 9(c)). The cross-sectional view of the optimized heterogeneous porous MBB beam is presented in Figure 9(d).

The iteration history of the porous topological optimization is plotted in Figure 10. The figure shows that the compliance of porous cantilever beam is optimized from 767.499 to 468.743,

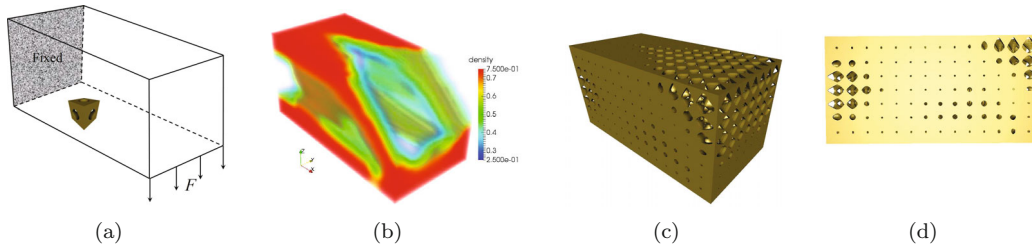


Figure 8 Porous topological optimization for P-type porous cantilever beam. (a) Design domain, boundary conditions and infilled porous element (P-type). (b) Optimized density distribution. (c) Optimized heterogeneous porous cantilever beam. (d) Cross-sectional view

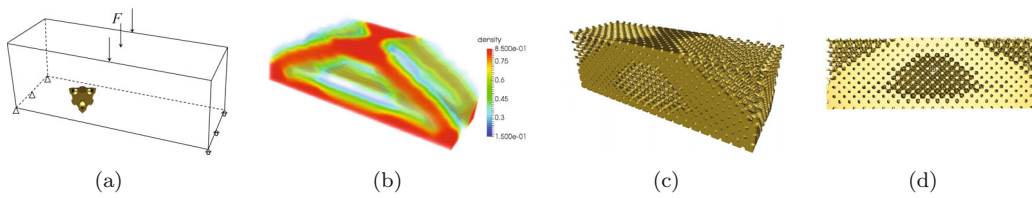


Figure 9 Porous topological optimization for D-type porous MBB beam. (a) Design domain, boundary conditions and infilled porous element (D-type). (b) optimized density distribution. (c) Optimized heterogeneous porous MBB beam. (d) Cross-sectional view

and the iteration takes 58 steps in total. The compliance of the porous MBB beam is optimized from 616.356 to 248.857, and the iteration takes 133 steps in total. Additionally, the iterations of the porous topological optimization for two beams both maintain a stable convergence.

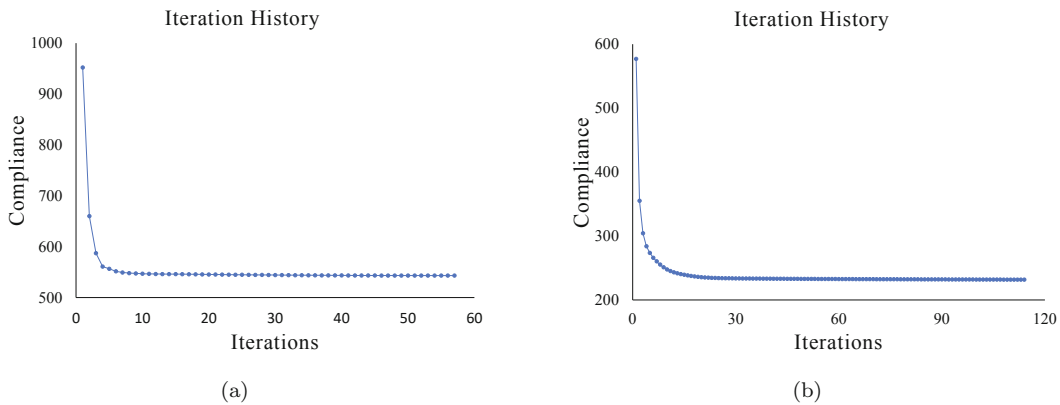


Figure 10 Iteration history. (a) Cantilever beam. (b) MBB beam

5.3 Comparison

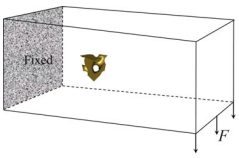
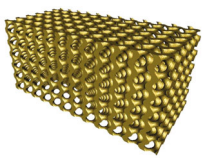
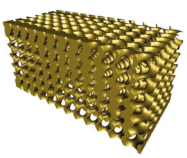
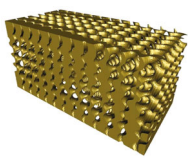
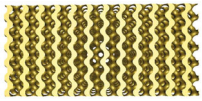
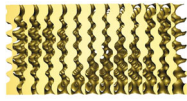
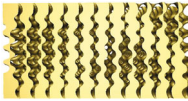
In this subsection, the proposed IGA-based porous topological optimization method is compared with an uniform method and the state of the art^[6], called scaled method.

We adopt a cantilever beam as an example to design G-type porous structures by using the above-mentioned three methods. The target volume fraction of the material is set as 0.3, and the density is constrained in the range of 0.2 to 0.8. Table 2 and Table 3 respectively present the G-type porous optimization structure of cantilever beam and tooth model, including their cross-sectional view, time of design and compliance value. The figures of the cross-sectional view show the connection of the porous elements generated by our method is smoother compared with the porous structure generated by the scaled method, which can better transfer the mechanical properties of the porous elements.

According to the time cost, our method is one order of magnitude faster than the scaled method because our method is based on IGA, which can significantly reduce the optimization variables. Specifically, the degree of freedom in the optimization of our method is $3 \times 21 \times 11 \times 11$. To keep the same nodes and continuity at each node of the cantilever beam with our method, the degree of freedom in the optimization of the scaled method is $3 \times 39 \times 19 \times 19$. Consequently, our IGA-based porous topological optimization method can effectively improve the ability of optimization.

Finally, we compare the compliance of the designed porous cantilever beams. The uniform method possesses the maximal compliance. Moreover, the compliance of the other two optimized porous structures is effectively reduced. However, in the scaled method, the structural properties of the infilled porous elements are not considered in the optimization. Therefore, our method can obtain the porous structures with minimum compliance value.

Table 2 Comparison of cantilever

	Uniform method	Scaled method	Our method
			
Cross-sectional view			
Optimization time(s)	-	5845.976	336.120
Compliance	1920.09	1089.93	840.495

The density distributions optimized by the scaled method and our method are shown in

Table 3 Comparison of tooth

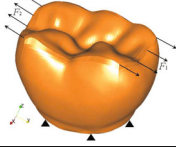
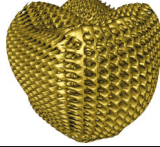
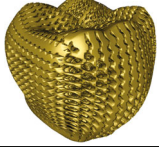

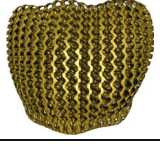
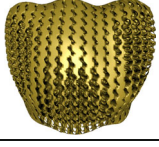
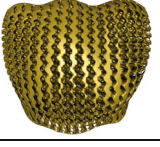
	Uniform method	Scaled method	Our method
			
Cross-sectional view			
Optimization time(s)	-	22936.11	329.16
Compliance	588085	196531	113879

Figure 11. A checkerboard phenomenon is shown in Figure 11(a). When constructing a porous structure, a critical post-processing is necessary for generating a scalar field by interpolating the optimized density distribution. Moreover, the scalar field needs to meet the constraint of the target volume fraction, which is a tough challenge. However, our IGA-based method can effectively avoid the process, which directly generates a smooth density distribution meeting specific requirements shown in Figure 11(b).

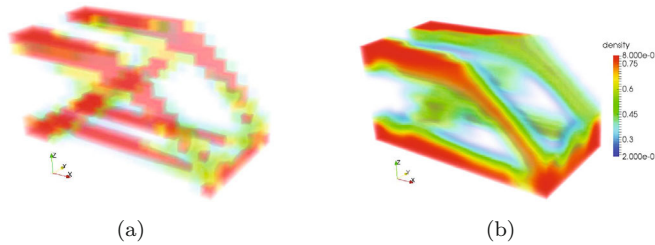


Figure 11 Optimized density distribution. (a) Scaled method. (b) Our method

In summary, the above-mentioned results indicate that the proposed method is suitable to design and optimize the porous structures.

5.4 Irregular Porous Domain

To design and optimize porous structures in an irregular domain, the design domain is discretised into hexahedral meshes, and then porous structures are generated by the mapping of porous elements, which solves two thorny issues. Firstly, an ideal hexahedral mesh model, which is suitable for finite element analysis, is difficult to generate. Secondly, some physical properties of the porous element will change before and after the mapping of the irregular domain, such as

the relative material density. Accordingly, the optimized porous structures cannot achieve the optimization requirements. However, the proposed IGA-based porous topological optimization method can solve the above-mentioned problems.

In Figure 12, a model of *Moai* is adopted in the IGA-based porous topological optimization, which is represented by a B-spline solid function with a degree of $2 \times 2 \times 2$ and control grid of $36 \times 12 \times 12$. The design domain and boundary conditions are depicted in Figure 12(a), in which the bottom of the model is fixed, and the external force is initially distributed over the top of the model. In the porous topological optimization, the target volume fraction is set to 0.4, and an I-WP-type porous element with a density of 0.16 to 0.85 intervals is selected to construct the porous structure. Consequently, the optimized density distribution is shown in Figure 12(b). Meanwhile, the optimized porous *Moai* infilled with $18 \times 6 \times 6$ I-WP-type porous elements and its cross-sectional view are shown in Figures 12(c) and 12(d).

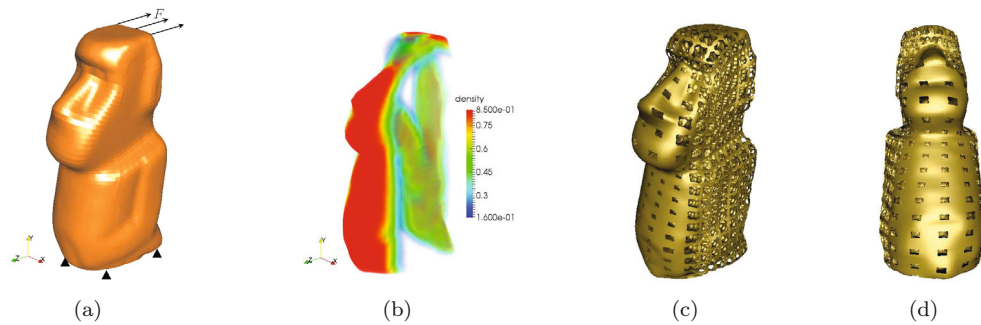


Figure 12 Porous topological optimization for I-WP-type porous *Moai*. (a) Design domain and boundary conditions. (b) Optimized density distribution. (c) Optimized heterogeneous porous *Moai*. (d) Cross-sectional view

Finally, we study the porous topological optimization issue of multiloads on the model of *Tooth* (Figure 13). Firstly, we provide a design domain and boundary conditions shown in Figure 13(a), in which the domain is represented by a solid B-spline function with a degree of $2 \times 2 \times 2$ and control grid of $20 \times 18 \times 18$, the bottom of the model is fixed, and two groups of external forces are initially distributed over the model. Subsequently, we set the target volume fraction to 0.3 and use the G-type porous element to perform optimization. Accordingly, the

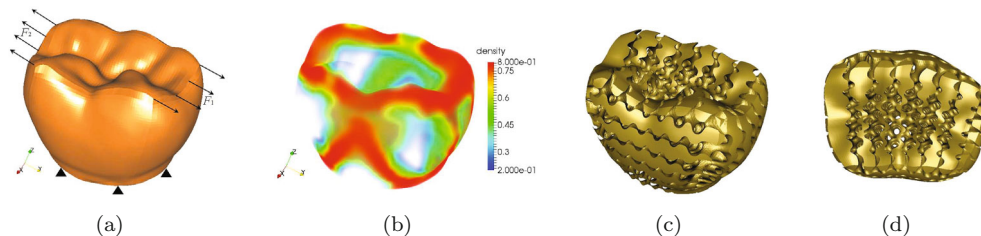


Figure 13 Porous topological optimization for G-type porous *Tooth*. (a) Design domain and boundary conditions. (b) Optimized density distribution. (c) Optimized heterogeneous porous *Tooth*. (d) Cross-sectional view

optimized density distribution (Figure 13(b)) and the optimized porous *Tooth* infilled with $7 \times 6 \times 6$ G-type porous elements (Figure 13(c)) are generated. Cross-sectional view of *Tooth* is presented in Figure 13(d).

6 Conclusion

In this study, we develop a practical IGA-based porous topology optimization method for designing optimized porous structures generated in a B-spline solid with TPMSs. The porous structure can achieve the mechanical performance requirements without increasing its weight by controlling the density distribution. Firstly, several types of porous elements with different densities using the implicit functions of TPMSs are designed. Secondly, an effective elastic modulus of the porous materials is defined and calculated on the basis of Energy Conservation Law. Subsequently, the functional relationships of different types of porous elements between the effective elastic modulus and the relative density are established. Thirdly, IGA-based porous topological optimization in the SIMP-framework is formulated. Finally, an optimum porous structure is generated in the B-spline solid with TPMS based on the optimized density distribution.

The equivalent elastic modulus of porous material is proposed and applied to the porous structural optimization by the method developed in this study, which takes account of the structural properties of the porous materials in the porous structural optimization and design. Furthermore, the porous topology optimization method in the SIMP-framework can effectively optimize the distribution of porous materials. Moreover, the structural heterogeneity of porous structures can be accurately demonstrated in the IGA-based optimization. In future work, the anisotropy of porous materials must be considered, and the influence of the B-spline solid mapping on the structural properties of porous structures must be eliminated, not only concerning the relative material density.

References

- [1] Elnasri I, Pattofatto S, Zhao H, et al., Shock enhancement of cellular structures under impact loading: Part I experiments, *Journal of the Mechanics and Physics of Solids*, 2007, **55**(12): 2652–2671.
- [2] Andrews E W and Gibson L J, The influence of cracks, notches and holes on the tensile strength of cellular solids, *Acta Materialia*, 2001, **49**(15): 2975–2979.
- [3] Ajdari A, Nayeb-Hashemi H, and Vaziri A, Dynamic crushing and energy absorption of regular, irregular and functionally graded cellular structures, *International Journal of Solids & Structures*, 2011, **48**(3–4): 506–516.
- [4] Wu S L, Liu X M, Yeung K W K, et al., Biomimetic porous scaffolds for bone tissue engineering, *Materials Science and Engineering: R: Reports*, 2014, **80**: 1–36.

- [5] Chen Y Z, Zhang R, Jiao L, et al., Metal-organic framework-derived porous materials for catalysis, *Coordination Chemistry Reviews*, 2018, **362**: 1–23.
- [6] Ajit P, Meisam A, Duncan H, et al., Strategies for functionally graded lattice structures derived using topology optimisation for Additive Manufacturing, *Additive Manufacturing*, 2018, **19**: 81–94.
- [7] Cheah C M, Chua C K, Leong K F, et al., Development of a tissue engineering scaffold structure library for rapid prototyping. Part 1: Investigation and classification, *International Journal of Advanced Manufacturing Technology*, 2003, **21**(4): 291–301.
- [8] Sun W, Starly B, Darling A, et al., Computer-aided tissue engineering: Application to biomimetic modelling and design of tissue scaffolds, *Biotechnology and Applied Biochemistry*, 2004, **39**(1): 49–58.
- [9] Rajagopalan S and Robb R A, Schwarz meets Schwann: Design and fabrication of biomorphic tissue engineering scaffolds, *Medical Image Analysis*, 2006, **10**(5): 693–712.
- [10] Schroeder C, Regli W C, Shokoufandeh A, et al., Computer-aided design of porous artifacts, *Computer-Aided Design*, 2005, **37**(3): 339–353.
- [11] Sogutlu S and Koc B, Stochastic modeling of tissue engineering scaffolds with varying porosity levels, *Computer-Aided Design and Applications*, 2007, **4**(5): 661–670.
- [12] Kou X Y and Tan S T, A simple and effective geometric representation for irregular porous structure modeling, *Computer-Aided Design*, 2010, **42**(10): 930–941.
- [13] Li M, Zhu L C, Li J Z, et al., Design optimization of interconnected porous structures using extended triply periodic minimal surfaces, *Journal of Computational Physics*, 2021, **425**: 109909.
- [14] Yoo D J, Porous scaffold design using the distance field and triply periodic minimal surface models, *Biomaterials*, 2011, **32**(31): 7741–7754.
- [15] Yang N, Quan Z, Zhang D W, et al., Multi-morphology transition hybridization cad design of minimal surface porous structures for use in tissue engineering, *Computer-Aided Design*, 2014, **56**: 11–21.
- [16] Hu C F and Lin H W, Heterogeneous porous scaffold generation using trivariate B-spline solids and triply periodic minimal surfaces, *Graphical Models*, 2021, **115**: 101105.
- [17] Hughes T J R, Cottrell J A, and Bazilevs Y, Isogeometric analysis: Cad, finite elements, nurbs, exact geometry and mesh refinement, *Computer Methods in Applied Mechanics and Engineering*, 2005, **194**(39): 4135–4195.
- [18] Zhang Y J, Bazilevs Y, Goswami S, et al., Patient-specific vascular nurbs modeling for isogeometric analysis of blood flow. *Computer Methods in Applied Mechanics and Engineering*, 2007, **196**(29): 2943–2959.
- [19] Martin T, Cohen E, and Kirby R M, Volumetric parameterization and trivariate B-spline fitting using harmonic functions, *Computer Aided Geometric Design*, 2009, **26**(6): 648–664.
- [20] Chen L, Xu G, Wang S Y, et al., Constructing volumetric parameterization based on directed graph simplification of l1 polycube structure from complex shapes, *Computer Methods in Applied Mechanics and Engineering*, 2019, **351**: 422–440.
- [21] Xu G, Kwok T H, and Wang C C L, Isogeometric computation reuse method for complex objects with topology-consistent volumetric parameterization, *Computer-Aided Design*, 2017, **91**: 1–13.
- [22] Aigner M, Heinrich C, Jüttler B, et al., Swept volume parameterization for isogeometric analysis, *Mathematics of Surfaces XIII*, Eds. by Edwin R H, Ralph R M, and Malcolm A S, Berlin, Heidelberg, 2009.

- [23] Xu G, Mourrain B, Wu X Y, et al., Efficient construction of multi-block volumetric spline parameterization by discrete mask method, *Journal of Computational and Applied Mathematics*, 2015, **290**: 589–597.
- [24] Xu G, Mourrain B, Duvigneau R, et al., Analysis-suitable volume parameterization of multi-block computational domain in isogeometric applications, *Computer-Aided Design*, 2013, **45**(2): 395–404.
- [25] Wang X L and Qian X P, An optimization approach for constructing trivariate B-spline solids, *Computer-Aided Design*, 2014, **46**: 179–191.
- [26] Lin H W, Jin S N, Hu Q Q, et al., Constructing B-spline solids from tetrahedral meshes for isogeometric analysis, *Computer Aided Geometric Design*, 2015, **35–36**: 109–120.
- [27] Hassani B, Khanzadi M, and Tavakkoli S M, An isogeometrical approach to structural topology optimization by optimality criteria, *Structural and Multidisciplinary Optimization*, 2012 **45**(2): 223–233.
- [28] Dedè L, Borden M J, and Hughes T J R, Isogeometric analysis for topology optimization with a phase field model, *Archives of Computational Methods in Engineering*, 2012, **19**: 427–465.
- [29] Wang Y J and Benson D J, Isogeometric analysis for parameterized LSM-based structural topology optimization, *Computational Mechanics*, 2016, **57**(1): 19–35.
- [30] Nguyen V P, Anitescu C, Bordas S P A, and Rabczuk T, Isogeometric analysis: An overview and computer implementation aspects, *Mathematics & Computers in Simulation*, 2015, **117**: 89–116.
- [31] Herrema A J, Wiese N M, Darling C N, et al., A framework for parametric design optimization using isogeometric analysis, *Computer Methods in Applied Mechanics & Engineering*, 2017, **316**: 944–965.
- [32] Qian X P, Topology optimization in B-spline space, *Computer Methods in Applied Mechanics & Engineering*, 2013, **265**: 15–35.
- [33] Liu H L, Yang D X, Hao P, et al., Isogeometric analysis based topology optimization design with global stress constraint, *Computer Methods in Applied Mechanics & Engineering*, 2018, **342**: 625–652.
- [34] Seepersad C C, Allen J K, McDowell D L, et al., Multifunctional topology design of cellular material structures, *Journal of Mechanical Design*, 2008, **130**(3): 499–513.
- [35] Nguyen J, Park S I, and Rosen D, Heuristic optimization method for cellular structure design of light weight components, *International Journal of Precision Engineering & Manufacturing*, 2013, **14**(6): 1071–1078.
- [36] Hu J B, Wang S F, Wang Y, et al., A lightweight methodology of 3D printed objects utilizing multi-scale porous structures, *The Visual Computer*, 2019, **35**: 1–11.
- [37] Brackett D, Ashcroft I, and Hague R, Topology optimization for additive manufacturing, *22nd Annual International Solid Freeform Fabrication Symposium — An Additive Manufacturing Conference*, University of Texas at Austin, 2011.
- [38] Wu J, Wang C C L, Zhang X T, et al., Self-supporting rhombic infill structures for additive manufacturing, *Computer-Aided Design*, 2016, **80**: 32–42.
- [39] Li D W, Dai N, Jiang X T, et al., Interior structural optimization based on the density-variable shape modeling of 3D printed objects, *The International Journal of Advanced Manufacturing Technology*, 2016, **83**(9–12): 1627–1635.
- [40] Li D W, Liao W H, Dai N, et al., Optimal design and modeling of gyroid-based functionally graded cellular structures for additive manufacturing, *Computer-Aided Design*, 2018, **104**: 87–99.

- [41] Zhang P, Toman J, Yu Y Q, et al., Efficient design-optimization of variable-density hexagonal cellular structure by additive manufacturing: theory and validation, *Journal of Manufacturing Science and Engineering*, 2015, **137**(2): 021004.
- [42] Wang X, Zhang P, Ludwick S, et al., Natural frequency optimization of 3d printed variable-density honeycomb structure via a homogenization-based approach, *Additive Manufacturing*, 2017, **20**: 189–198.
- [43] Li D W, Dai N, Tang Y L, et al., Design and optimization of graded cellular structures with triply periodic level surface-based topological shapes, *Journal of Mechanical Design*, 2019, **141**(7): 071402.
- [44] Gandy P J F, Bardhan S, Mackay A L, et al., Nodal surface approximations to the P, G, D and I-WP triply periodic minimal surfaces, *Chemical Physics Letters*, 2001, **336**(3): 187–195.
- [45] Doi A and Koide A, An efficient method of triangulating equivalued surfaces by using tetrahedral cells, *IEICE Transactions on Information and Systems*, 1991, **74**(1): 214–224.
- [46] Bendsøe M P, *Optimization of Structural Topology, Shape, and Material*, Springer, Berlin, 1995.
- [47] Bendsøe M P and Sigmund O, Material interpolation schemes in topology optimization, *Archive of Applied Mechanics*, 1999, **69**(9–10): 635–654.
- [48] Heath M T, *Scientific Computing: An Introductory Survey*, 2nd Edition, Society for Industrial and Applied Mathematics, Philadelphia, 2018.

Appendix A

Functional relationships between the relative density and the threshold constant (the correlation coefficients equal 1).

P-type: $\rho = -0.2576C + 0.5$;

D-type: $\rho = -0.3518C + 0.5$;

G-type: $\rho = -0.2937C + 0.5$;

I-WP-type: $\rho = -0.0221C^3 + 0.0395C^2 - 0.3267C + 0.4681$.

Appendix B

Functional relationships between the equivalent ratio of elastic modulus and the relative density (the correlation coefficients greater than 0.999).

P-type: $E^*/E = -0.3833\rho^3 + 1.5493\rho^2 - 0.1648\rho - 0.0021$;

D-type: $E^*/E = 1.1654\rho^2 - 0.1929\rho + 0.0164$;

G-type: $E^*/E = 1.1453\rho^2 - 0.1683\rho + 0.0095$;

I-WP-type: $E^*/E = 0.5446\rho^3 + 0.1094\rho^2 + 0.3466\rho - 0.0082$.